Journal of
Applied
Crystallography
ISSN 0021-8898

Received 25 January 2013
Accepted 20 April 2013

Relationship between performance and microvoids of aramid fibers revealed by two-dimensional small-angle X-ray scattering

Caizhen Zhu,[a,b] Xiaofang Liu,[a] Jing Guo,[a] Ning Zhao,[a] Changsheng Li,[a] Jie Wang,[c] Jianhong Liu[b] and Jian Xu[a]*

[a]Institute of Chemistry, Chinese Academy of Sciences, Beijing 100190, People's Republic of China, [b]Shenzhen Key Laboratory of Functional Polymers, College of Chemistry and Chemical Engineering, Shenzhen University, Shenzhen 518060, People's Republic of China, and [c]Shanghai Synchrotron Radiation Facility, Shanghai Institute of Applied Physics, Shanghai 201204, People's Republic of China. Correspondence e-mail: jxu@iccas.ac.cn

Although the crystal structure in aramid fibers and the relationship between the size and orientation of crystallites and the performance of a material have been explored in detail, the effect of microvoids in an aramid fiber on its performance is still not clear. However, it is known that the mechanical properties depend strongly on the fiber morphology. In the present research, two-dimensional small-angle X-ray scattering is applied to characterize the microvoids in aramid fibers. Pauw's two-dimensional full pattern fitting method and scattering model have been enhanced by introducing orientation parameters, such as zenith angle distribution and azimuthal angle distribution, and instrumental parameters like point spread function and beam profile function. A series of aramid fibers with different strengths were studied using the new two-dimensional full pattern fitting method to extract the microvoid parameters from the scattering patterns. The results show that the microvoids in the aramid fiber affect the fiber strength directly. The greater the number of spherical microvoids and the larger the ellipsoidal microvoids, the weaker the aramid fiber.

1. Introduction

Aramid fibers are a class of high-performance synthetic fiber with many outstanding properties, such as high strength, high tenacity, high modulus, high heat resistance, low density and low flammability, which neither melt nor ignite in normal levels of oxygen. An aramid fiber is a long-chain synthetic polyamide in which at least 85% of the amide (–CO—NH–) linkages are attached directly between two aromatic rings (Mark, 2004). The synergism effect between rigid aromatic rings and intermolecular hydrogen bonds jointly straightens the molecular chain to form molecular lamellae, and then these molecular lamellae stack layer by layer, resulting in a very high degree of crystallinity.

Poly(*p*-phenylene terephthalamide) (PPTA) is one of the most important aramid fibers. In PPTA fibers, the paracrystalline grains have a unit cell with dimensions $a = 7.88$, $b = 5.22$, $c = 12.9$ Å, $\gamma \simeq \alpha = \beta = 90^\circ$, where the c axis is parallel to the fiber axis (Hindeleh & Abdo, 1989; Hindeleh *et al.*, 1984). What kind of molecular-chain symmetry is adopted in single-crystal PPTA has been the subject of debate for many years. Liu *et al.* (1996) used the confined thin-film melt polymerization technique to cultivate lamellar single crystals, and determined that the molecular chains adopt the $P1a1$ rather than either of the Pn or $P2_1/n$ space groups. Then Gardner *et al.* (2004) and Plazanet *et al.* (2005) validated the model with neutron fiber diffraction, neutron vibrational spectroscopy and density functional theory calculations. It was found that the paracrystalline grains arranged themselves radially along the cross section and constructed pleated sheets along the fiber axis.

The performance of aramid fibers is closely related to their internal structure. As early as 1977, Northolt and co-workers (Northolt & van Aartsen, 1977; Northolt & Hout, 1985; Northolt, 1981) investigated fiber compliance with respect to the chain axis distribution and attempted to establish an equation to describe their relationship. Young *et al.* (1992) studied the structure and mechanical properties of a series of well characterized aramid fibers with transmission electron microscopy and Raman microscopy. Their results showed that the fiber modulus is controlled by the molecular orientation, and that the fiber strength reduces when a highly oriented skin region is present. With the help of wide-angle X-ray diffraction, Rao (2001) evaluated the orientation angle, lattice constants, paracrystalline parameter and apparent degree of crystallinity of PPTA fibers and found that the fiber modulus was determined by a combination of crystallite orientation and paracrystalline parameter. Kotera *et al.* (2007) also measured the elastic modulus of the crystalline regions of a single PPTA fiber in the direction parallel to the chain axis by X-ray diffraction and *in situ* tensile testing. Davies *et al.* (2008)

studied the PPTA fiber cross section with on-axis mesh scans by combined small-angle X-ray scattering (SAXS) and wide-angle X-ray scattering, and confirmed that the aramid fiber had a radial texture of crystalline domains with different orientation orders at skin, central core and intermediate layers.

Microvoids also exist in aramid fibers, although there are some opposed views, arguing that the streak SAXS signal only comes from the fibril (Ran *et al.*, 2001; Grubb *et al.*, 1991). Dobb *et al.* (1979) found that the voids appear to be located mainly around the periphery of the fibers. Aerts (1991) has verified the existence of microvoids by depositing Ag_2S into the microvoids. Mooney & MacElroy (2004) conducted differential water vapor sorption experiments on Kevlar49 and demonstrated the presence of the microvoids from another aspect. Recently, Pauw, Vigild, Mortensen, Andreasen & Klop (2010) studied the microvoid variation in aramid fibers before and after heat treatment with two-dimensional SAXS, which is an effective tool for the characterization of microvoids; the scattering patterns were analyzed by a two-dimensional full pattern fitting method. Pauw, Vigild, Mortensen, Andreasen & Klop (2010) also summarized the proof for the existence of microvoids in aramid fibers: the density of the fiber is lower than the crystalline density of PPTA; there is no apparent amorphous diffraction signal in the two-dimensional diffraction pattern; and the SAXS signal is quite strong and is likely to arise from an electron density difference not between amorphous and crystal structure but between microvoid and crystal structure. It was proved that microvoids are also present in other high-performance fibers, such as ultra-high-molecular-weight polyethylene fiber (Humbert *et al.*, 2010) and carbon fiber (Zhu *et al.*, 2012).

Although a great deal of effort has been made to study the structure and properties of PPTA fiber, the effect of the microvoids on its performance has not yet been comprehensively explored. In the present research, we first adapt Pauw's two-dimensional full pattern fitting method by introducing orientation parameters, zenith angle distribution and azimuthal angle distribution, and instrumental parameters like point spread function and beam profile function, which may smear the scattering pattern. In order to describe the isotropic scattering in some samples, spherical scatterers are added to the model; this is evolved to a dual model, containing two kinds of scatterers, ellipsoidal and spherical. With this adaptation, microvoids in a series of aramid fibers with different mechanical performance are analyzed, and finally the relationship between the fiber tensile strength and the microvoid parameters is established.

2. Experiments

2.1. Samples

The samples were supplied by Yantai Tayho Advanced Materials Company Ltd, China, and the mechanical properties of the aramid fiber bundles are listed in Table 1. These aramids are as-spun samples without heat treatment.

Table 1
Mechanical properties of the aramid fibers.

1 dtex = 0.1 mg m^{-1}.

Sample	Strength (*cN*/dtex)	Modulus (*N*/dtex)	Elongation (%)
A	9.16 (2)	44.39 (25)	2.370 (2)
B	12.25 (4)	56.22 (52)	2.370 (1)
C	14.75 (4)	52.26 (35)	2.840 (2)
D	16.46 (3)	43.94 (8)	3.830 (3)
E	18.72 (3)	57.93 (46)	3.520 (1)
F	20.43 (6)	61.63 (33)	3.570 (3)

2.2. Two-dimensional SAXS experiment

The fiber bundles were dried before the measurement and straightened when mounted on an auto sample stage which was controlled remotely. The sample stage was adjusted to the X-ray beam path before use with the assistance of an X-ray fluorescence screen, a video collection system and a CCD detector (mar165, Marresearch, Germany). During the experiment, the aramid fiber bundles were exposed to X-rays for 10 s. All SAXS patterns were corrected for X-ray flux fluctuations, background X-ray scattering from air and detector dark current. The bundles of aramid fibers were very loose because no surface treatment with sizing agent was applied. Although we straightened out the fibers as far as possible with a comb and by hand before fixing them onto the sample stage, it was hard to measure the thickness of the fiber through which the X-ray beam passed. Therefore the X-ray scattering patterns were not calibrated by the thickness of the sample, so it is hard to compare the microvoid content in different fibers through the comparison of the SAXS integral invariant (Glatter & Kratky, 1982) or scattering intensity. Winding a fiber onto a frame is an effective way of sample preparation (Hermans *et al.*, 1959). However, for the present research, the fiber is a little loose and the X-ray spot size is relatively small at the location of the sample stage. Therefore, Hermans's sample preparation method was also unable to solve the problem; this is discussed in the supporting information.[1]

The SAXS experiment was performed at beamline BL16B1 at Shanghai Synchrotron Radiation Facility (SSRF) in Shanghai, China, with a photon energy of 10 keV and a wavelength of 0.124 nm. There are two ionization chambers, which are able to read the real-time intensity of the X-ray flux before and after the fiber. The CCD was placed at a distance of 5073 mm away from the samples, calibrated by the X-ray diffraction from dried cattle tendon with its standard periodicity, and the distance was also checked by a measuring tape.

3. Theory

3.1. Two-dimensional SAXS model

A SAXS pattern is the collection of the signal in reciprocal space, while the parameters of the microvoids are needed in

[1] Supplementary material for this paper is available from the IUCr electronic archives (Reference: HE5593). Services for accessing this material are described at the back of the journal.

real space. Immense advances have been made in extracting the structure information for an isotropic system, but for an anisotropic system, there is still a great deal to be explored. As Stribeck (2007) says '...in the field of anisotropic materials we are presently in a similar situation as science has been in 1931 in respect to isotropic data...'. To solve this issue, analysis methods such as the streak method (Stribeck, 2007; Thünemann & Ruland, 2000; Perret & Ruland, 1970), the interface distribution function (Ruland, 1977; Stribeck & Ruland, 1978; Ruland, 1978; Stribeck, 2004), the chord length distribution function (Stribeck, 2007; Stribeck *et al.*, 2008), the full pattern method (Pauw, Vigild, Mortensen, Andreasen & Klop, 2010; Fischer *et al.*, 2010; Engel *et al.*, 2009), and the correlation method (Kortleve & Vonk, 1968; Vonk, 1979) have all been devised.

Scattering curves can be obtained by slice or projection along one direction or in multiple directions and then analyzed by model fitting or a model-free method, such as *via* Guinier's law, Porod's law and other theoretical derivations. These methods based on scattering curves inevitably leave many data points on the scattering pattern unused and lose too much information. Nowadays, the full pattern fitting method, using almost all data points on the scattering pattern, is preferred as a candidate method for analyzing scattering patterns of an anisotropic system. However, the previous two-dimensional SAXS models have not taken zenith angle (θ in Fig. 1) distribution, azimuthal angle (φ in Fig. 1) distribution or instrumental parameters into account. The zenith angle distribution and azimuthal angle distribution affect the scattering intensity (Engel *et al.*, 2009), which can also be seen from equations (2) and (8), while the instrumental parameters smear the scattering pattern (Suhonen *et al.*, 2005), as discussed in the supporting information. The variance of the size distribution and the nonideal nature of the instrument have a similar effect on the scattering pattern, all blurring the pattern. If the model does not take instrumental parameters into account, then we need to increase the variance of the distribution to account for the smearing, but this may introduce errors when we compare two distributions whose mean values are close.

In aramid fibers, microvoids are a minority and are situated randomly; therefore, microvoids can be thought of as a typical

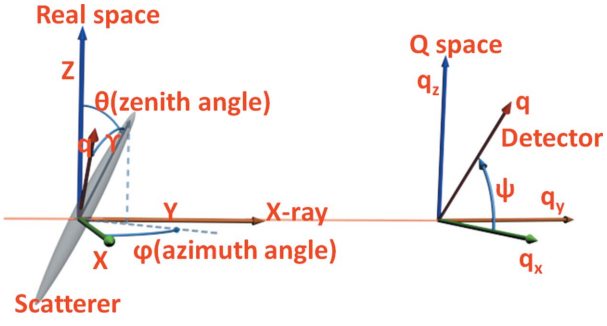

Figure 1
A schematic diagram showing the scatterer, the detector and their geometric relationship.

dilute system which means that one microvoid is relatively far from the others. Hence, the scattering intensity can be written as

$$I(\mathbf{q}) = \sum_{n=1}^{N} F_n^2. \tag{1}$$

Equation (1) indicates that the total scattering intensity is the summation of the intensity scattered by each microvoid. For a dilute system, this is a straightforward but effective simplification which has been used in a number of methods (Pauw, Vigild, Mortensen, Andreasen & Klop, 2010; Fischer *et al.*, 2010). When the scatterer is an ellipsoidal microvoid, the X-ray scattering form factor can be written as

$$F(q, \psi, R_1, R_2) = 3\frac{\sin(qR_{\rm ell}) - qR_{\rm ell}\cos(qR_{\rm ell})}{(qR_{\rm ell})^3}. \tag{2}$$

Here $R_{\rm ell}$ is equal to $(R_1^2\sin^2\gamma + 4R_2^2\cos^2\gamma)^{1/2}$, the angles ψ and γ are defined in Fig. 1, and R_1 and R_2 are the radii of the semi-major and semi-minor axes of the ellipsoidal microvoid. A lognormal distribution was used to simulate the distribution of semi-major and semi-minor radii:

$$f(R) = \frac{1}{R\sigma(2\pi)^{1/2}}\exp\left[\frac{-(\ln R - \mu)^2}{2\sigma^2}\right]. \tag{3}$$

Here μ and σ are the parameters of the lognormal distribution, and the mean m and variance υ can be calculated through μ and σ:

$$m = \exp(\mu + \sigma^2/2), \tag{4}$$

$$\upsilon = \exp(2\mu + \sigma^2)(\exp\sigma^2 - 1). \tag{5}$$

Aramids have a high degree of crystallinity, and the crystalline grains arrange along the fiber axis, with the result that the ellipsoidal microvoids are also oriented along the fiber axis. Generally, microvoids are not strictly parallel to the fiber axis, and the Von Mises distribution, also known as a circular normal distribution, as defined in equation (6), is used to simulate the zenith angle distribution:

$$h(\theta \mid \theta_0, \kappa) = \frac{\exp[\kappa\cos(\theta - \theta_0)]}{2\pi I_0(\kappa)}. \tag{6}$$

Here $h(\theta \mid \theta_0, \kappa)$ is the Von Mises distribution function centered at θ_0 with the shape factor defined by κ; $I_0(\kappa)$ is the modified Bessel function of order zero.

In common with other kinds of fibers, aramid fibers have rotational symmetry, which means that scattering patterns obtained from different directions perpendicular to an aramid fiber are identical. We use a uniform distribution to simulate this characteristic. Some methods ignore the distribution due to the rotational symmetry, but this characteristic definitely affects the scattering pattern, as can be seen in the final relation between different angles [equation (8)].

According to the above discussion, the scattering intensity can be written as

Table 2
Parameters used in full pattern fitting.

Parameter	q_{max} (Å^{-1})	q_{min} (Å^{-1})	Circle	Content (%)	S_x (Å^{-1})	S_z (Å^{-1})	S_x^{PSF} (Å^{-1})	S_z^{PSF} (Å^{-1})	α	d	c
Value	0.14	0.04	100	0.5	0.0004	0.0003	0.00007	0.00007	0.35	10	1.5

$$I(q,\psi) = C_1 \int_0^{\infty}\int_0^{\infty} V(R_1,R_2)^2 \left[\int_{-\pi/2}^{\pi/2} h(\theta)\sin\theta\,\mathrm{d}\theta \int_0^{2\pi} g(\varphi)\,\mathrm{d}\varphi \times F^2(q,R_1,R_2,\theta,\varphi,\psi) f(R_1) f(R_2) \right] \mathrm{d}R_1\,\mathrm{d}R_2. \quad (7)$$

Here $I(q,\psi)$ is the measured intensity, $V(R_1,R_2)$ is the volume of a scatterer with semi-major and semi-minor radii R_1 and R_2, $h(\theta)$ is the zenith angle distribution function, $g(\varphi)$ is the azimuthal angle distribution function, the angles θ, γ, φ and ψ are defined in Fig. 1, and C_1 is a scale factor. The relationship between the different angles can be written as

$$\cos\gamma = \cos\theta\sin\psi + \sin\theta\cos\psi\cos\varphi. \quad (8)$$

We used a two-dimensional Gaussian function $W(q_x,q_z)$ to simulate the X-ray beam profile:

$$W(q_x,q_z) = \frac{1}{2\pi S_x S_z}\exp\left[-\frac{1}{2}\left(\frac{q_x}{S_x}\right)^2\right]\exp\left[-\frac{1}{2}\left(\frac{q_z}{S_z}\right)^2\right]. \quad (9)$$

Here q_x and q_z are the components of the scattering vector in the detector plane, as depicted in Fig. 1, and S_x and S_z are the variances of the two-dimensional Gaussian function along the directions q_x and q_z.

The CCD detector is also not an ideal detector, and the deviation could be described by a point spread function (PSF). In terms of the mar165 CCD's specification, a two-dimensional Gaussian function with a tail function was used to describe the PSF, as shown in equation (10):

$$W_{PSF}(q_x,q_z) = \frac{1}{2\pi S_x^{PSF} S_z^{PSF}}\exp\left[-\frac{1}{2}\left(\frac{q_x}{S_x^{PSF}}\right)^2\right] \times \exp\left[-\frac{1}{2}\left(\frac{q_z}{S_z^{PSF}}\right)^2\right] + \frac{c}{(1+q^2d^2)^{\alpha}}. \quad (10)$$

The tail function promotes full fitting according to the results of Pontoni *et al.* (2002). Here $W_{PSF}(q_x,q_z)$ is the PSF function, S_x^{PSF} and S_z^{PSF} are the variances of the two-dimensional Gaussian function along the directions q_x and q_z, and c, d and α are three parameters defining the tail function; the values of these parameters are listed in Table 2.

In some aramid fibers, evident isotropic scattering is expected, so additional spherical scatterers are added to the calculation and the model evolves to a dual model, as shown in Fig. 2. The form factor of a sphere is relatively simple, and it is expressed as

$$F(q,R) = 3\frac{\sin(qR) - qR\cos(qR)}{(qR)^3}. \quad (11)$$

Here R is the radius of the spherical microvoid. The intensity then can be defined as

$$I_{total} = C_1 I^1_{ellipsoid} + C_2 I_{sphere}, \quad (12)$$

where C_1 and C_2 are scaling factors and $I^1_{ellipsoid}$ and I_{sphere} are the calculated intensities of the ellipsoid-like and sphere-like microvoid types.

The fibrillar structure also generates SAXS signal, but the fibril is about an order of magnitude longer and thicker than the microvoid. According to the law of reciprocity, the larger the scatterer, the lower the scattering angle of the SAXS signal located at the detector. Hence, the fibrillar structure produces the SAXS signal at the lowest angle (Pauw, Vigild, Mortensen, Andreasen, Klop, Breiby & Bunk, 2010). There is a wide difference in size between the microvoid and the fibril, so their SAXS signals can be separated – a larger ellipsoid to model the fibril and a smaller ellipsoid to model the microvoid; then the scattering intensity is

$$I_{total} = C_1 I^1_{ellipsoid} + C_3 I^2_{ellipsoid} + C_2 I_{sphere}, \quad (13)$$

where C_3 is a scaling factor and $I^2_{ellipsoid}$ is the scattering intensity of the fibril.

3.2. Two-dimensional full pattern fitting method

On the basis of the two-dimensional SAXS model mentioned above, the two-dimensional full pattern fitting method was employed to extract the parameters of the scatterers through minimizing the residual function diff:

$$\mathrm{diff} = \frac{\sum_{i=1}^{N}[\log I_{sim}(q_x,q_z) - \log I_{exp}(q_x,q_z)]^2}{N-n}, \quad (14)$$

where N is the number of the pixel involved during the two-dimensional full pattern fitting, n is the number of parameters, i is the datapoint index, I_{sim} is the scattering intensity obtained from the two-dimensional model and I_{exp} is the experimental scattering intensity. A schematic diagram of the two-dimensional full pattern fitting method is shown in Fig. S-1 in the supporting information; the method regulates the parameters involved in the model so that the resulting simulated two-

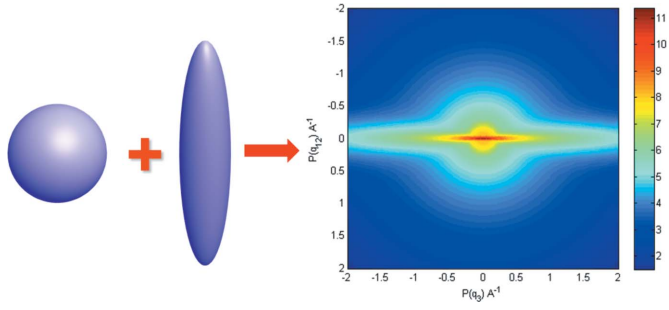

Figure 2
A schematic diagram of the dual model.

dimensional SAXS pattern gets closer and closer to the experimental two-dimensional SAXS pattern.

4. Results and discussion

4.1. Two-dimensional SAXS

Fig. S-2(*a*) shows an ideal scattering pattern when the sample is illuminated by an ideal point X-ray source and the signal is collected by an ideal detector. Actually, we can use the two-dimensional Gaussian function as expressed in equation (9) to describe the dispersion of the X-ray beam at a certain distance; hence the variances in the q_x and q_z directions are found to be 0.00040 (2) and 0.00030 (2) Å^{-1} according to the instrument parameters.

In addition, the scattering pattern is smeared by the CCD (Pontoni *et al.*, 2002; Uesugi *et al.*, 2011; Du & Voss, 2004). This effect can be described by a PSF. According to its technical specifications, the full width at half-maximum of the PSF of the CCD at SSRF (mar165, Marresearch, Germany) is 100 µm and the intensity falls to about 1% of the peak intensity at a spread of 300 µm, forming a tail. We used the parameters given by the detector technical specification to calculate the PSF.

A two-dimensional Gaussian function with a tail, as expressed in equation (10), is used to simulate the PSF, and the corresponding parameters are listed in Table 2, where $S_x^{\rm PSF}$ and $S_z^{\rm PSF}$ describe the spreads of the two-dimensional Gaussian function, and α, d and c describe the tail function. To improve the efficiency of calculation, the experimental patterns were linearly binned with bins containing 4 × 4 image pixels.

The real beam profile and the beam profile used in the model are compared in Figs. S-2(*c*) and S-2(*d*) in the supporting information. The shape and size of the calculated beam profile get very close to the real values, which indicates that the values used to describe the beam profile and PSF are reasonable.

Fig. S-2(*b*) is the ideal scattering pattern smeared by the PSF and beam profile. When the scattering pattern is convoluted with these functions, the scattering ripples fall into a decline. The scattering curves were sliced along the meridional and equatorial directions, as shown in Figs. S-3(*a*) and S-3(*b*) in the supporting information, from which we can see that the smearing has more effect on the meridional direction than on the equatorial direction.

The parameters of the beam profile and the PSF are listed in Table 2. The grid length $q_{\rm min}$ and maximum value $q_{\rm max}$ of the scattering vector were set to 0.04 and 0.14 Å^{-1}, respectively, during the two-dimensional scattering model calculation. Each scattering pattern was simulated 100 times, optimized to convergence. All instrument parameters were fixed during the modeling and two-dimensional fitting. As mentioned previously, it is not easy to determine the thickness of a fiber along the beam path precisely. Hence the microvoid content has been fixed (microvoid content = 0.5%) during the fitting. The value of the microvoid content only scales the scattering intensity but does not reshape the scattering pattern when the microvoid is a minority. The microvoid content is controlled by the number of microvoids, the size of the microvoids, the difference electron density and the volume of the system used in the two-dimensional SAXS model.

The scattering patterns of various aramid fibers are depicted in Fig. 3; these patterns have been calibrated for X-ray beam flux fluctuation, background X-ray scattering and detector dark current. The tensile strength of the fibers increases through the sequence of sample identifiers A–B–C–D–E–F, as shown in Fig. 3. All bundles of aramid fibers were mounted horizontally. As shown in Fig. 3, the scattering intensity decreases with the increase of fiber strength, especially the isotropic scattering intensity. The two-dimensional SAXS model and two-dimensional full pattern fitting method mentioned above were applied to extract information on the scatterers in the fiber. Owing to the obvious isotropic scattering in samples A, B and C, as shown in Figs. 3(*a*), 3(*b*), 3(*c*), a dual model was used to analyze these scattering patterns.

The anisotropic scattering intensity in all bundles of fibers, as shown in Fig. 3, is very narrow in the meridional direction, which indicates that the ellipsoidal scatterers are arranged almost parallel to the fiber axis. This result is the same as that obtained for the as-spun aramid fiber reported by Pauw and co-workers but is different from those for heat-treated aramid fiber (Pauw, Vigild, Mortensen, Andreasen & Klop, 2010) and other kinds of fibers, such as carbon fiber (Zhu *et al.*, 2012). The zenith angle distribution function was adjusted first, and we found that the distribution is narrow enough, *i.e.* fits the scattering pattern well, when the mean value of the orientation angle (θ_0) is 0 and the shape factor of the distribution (κ) is 700. Hence these values were fixed during the two-dimensional fitting and the corresponding Von Mises distribution is shown in Fig. 4(*d*).

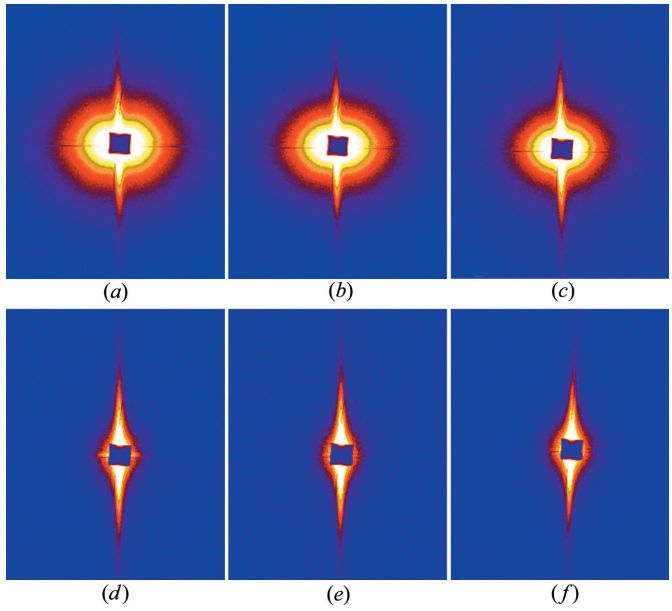

Figure 3
Two-dimensional SAXS patterns of different aramid fibers. The bundles of fibers are mounted horizontally. Intensity is shown on a logarithmic scale. (*a*) Sample A, (*b*) sample B, (*c*) sample C, (*d*) sample D, (*e*) sample E and (*f*) sample F.

To describe the SAXS signal at low angle resulting from the fibrillar structure (Pauw, Vigild, Mortensen, Andreasen & Klop, 2010), a large ellipsoid was added to the model as described above. The information on microvoids and fibrils can be separated because of their significant difference in size, and the isotropic scattering signal obviously does not come from the fibrils, because the fibrils are all parallel to the fiber axes. To reduce the number of parameters, the variance of the long- and short-axis radii of the fibril was set to 3 Å and fixed during the fitting. After two-dimensional fitting of sample C, as shown in Fig. 3(*c*), we obtained the lengths of the semi-major and semi-minor axes of the fibril. To further reduce the number of parameters, the size of the fibril was fixed during the following fitting. This approximation method is reasonable taking microvoid and fibril SAXS signal in different regions into account, and it is also adopted by Pauw, Vigild, Mortensen, Andreasen & Klop (2010). We have made a substantial effort to fix as many parameters as possible in the model and reduce the number of parameter during the fitting. These reductions make the model more stable and reliable.

Fig. 4 shows the results of full fitting of aramid fiber C. The calculated pattern is shown in Fig. 4(*a*), which scales logarithmically. For convenience of comparison, the experimental pattern and calculated pattern are stacked in Fig. 4(*b*), where the figure scales logarithmically. From this figure we can see that the calculated pattern is approaching the experimental scattering pattern. Fig. 4(*c*) shows the residual of the two scattering patterns, from which we can see that the residual is small, implying that the dual model is suited to describing the scatterer in these samples.

The size and orientation parameters are depicted in Fig. 4(*d*), where the red line is the ideal distribution described

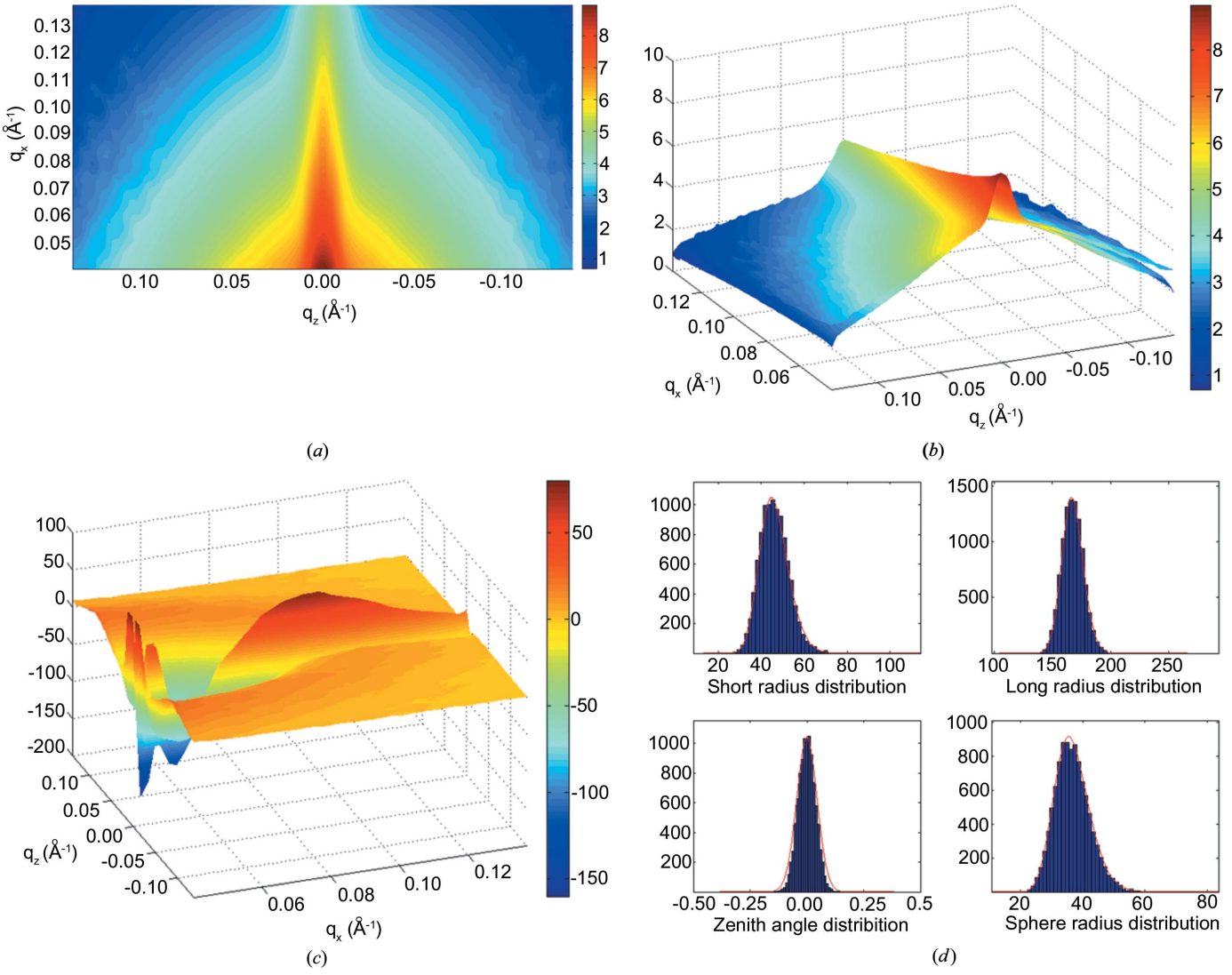

Figure 4
Full pattern fitting of sample C. (*a*) The calculated pattern, (*b*) the experimental pattern and calculated pattern superimposed, (*c*) the residual of the experimental pattern and the calculated pattern, and (*d*) the parameters of the microvoids used in the model, where the red line is the theoretical distribution defined by the parameters and the histogram shows the real values used in the program generated randomly. Patterns (*a*) and (*b*) are shown on a logarithmic scale.

Table 3
The parameters of different aramid fibers.

R_S and VR_S are the mean value and the variance of the short-axis distribution, respectively; R_L and VR_L are the mean value and the variance of the long-axis distribution; R is the mean value of sphere radius; VR is the variance of the sphere radius distribution; diff is the residual between the experimental scattering pattern and the scattering pattern calculated by the model.

	R_S (Å)	VR_S (Å)	R_L (Å)	VR_L (Å)	R (Å)	VR (Å)	diff
A	53.5	54.3	178.5	88.7	42.3	33.2	0.29
B	46.3	41.7	180.3	86.4	38.5	28.7	0.21
C	46.2	45.3	167.5	83.5	36.7	31.3	0.21
D	42.1	74.5	156.4	78.5	0	0	0.18
E	34.5	34.8	145.4	77.8	0	0	0.14
F	33.2	40.5	131.4	82.3	0	0	0.14

by the parameters and the histograms are the data sampling used in the two-dimensional model. A series of random numbers controlled by the distribution was generated to represent the distribution during the two-dimensional SAXS calculation. The histograms get very close to the distribution described by the red line, which means that the generated random number is reasonable and sufficient. In sample C, the radius of the long axis is 167.5 Å and the radius of the short axis is 46.2 Å, and the ellipsoidal scatterers arrange themselves almost parallel to the fiber axis. Spherical scatterers also exist in sample C, with a radius of about 36.7 Å. The long- and short-axis radii of the large ellipsoid used to describe the fibrillar structure are 965.1 and 165.5 Å, respectively. These values were fixed during the other two-dimensional fits because the SAXS signal of a large ellipsoidal scatterer is mainly located at low angles. Therefore, this is a reasonable approximation in the present work.

The size, distribution and orientation parameters obtained by using the same process to fit samples A, B, D, E and F are listed in Table 3. The scattering patterns of D, E and F were fitted only with ellipsoids owing to the absence of isotropic scattering, so the sphere radius of the scatterer in D, E and F is zero.

Fig. 5 shows the parameters of the microvoids in the samples, and the tensile strength of the fiber is also depicted in the figure for comparison. As mentioned above, the mean value of the orientation angle between the fiber axis and the long axis of the ellipsoidal microvoids is zero in each sample, as shown in Fig. 5(*a*). The short-axis radii of the ellipsoidal microvoids decrease as the fiber strength increases (Fig. 5*b*),

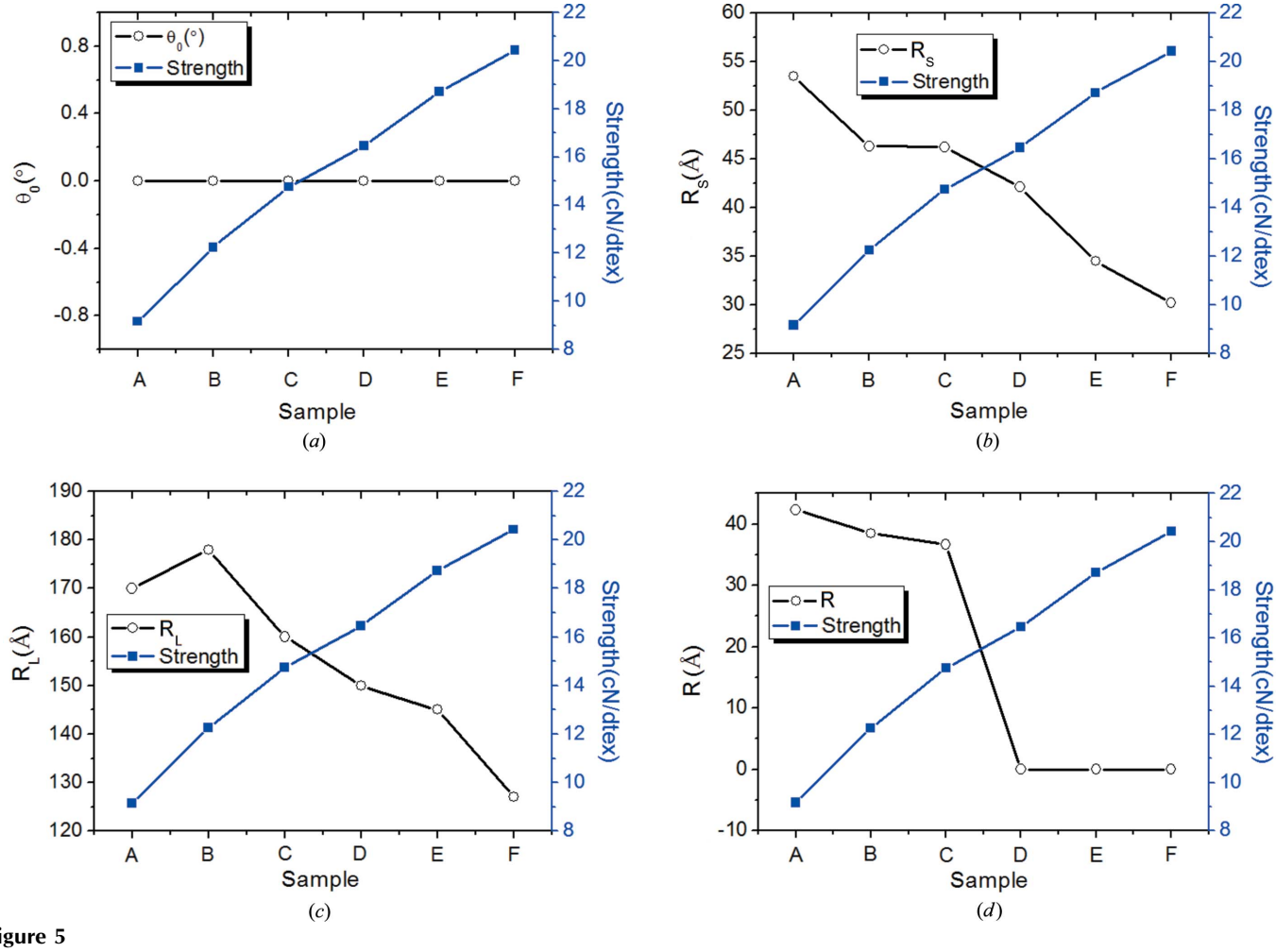

Figure 5
The parameters of microvoids in the aramid fibers. (*a*) Orientation angle, (*b*) radius of the short axis, (*c*) radius of the long axis and (*d*) radius of the sphere.

where the short-axis radii of A, B, C, D, E and F are 53.5, 46.3, 46.2, 42.1, 34.5 and 33.2 Å, respectively. Among these samples, sample A has the lowest strength and the short-axis radius of its microvoids is also the largest one. Conversely, sample F has the shortest axis and the highest strength. The largest short-axis radius (A) is about 20 Å larger than the smallest one (F).

The change of the long-axis radius of the microvoid with fiber strength follows a similar principle to that of the short-axis radius, except for sample B, as shown in Fig. 5(*c*), where the long-axis radii of samples A, B, C, D, E and F are 178.5, 180.3, 167.5, 156.4, 145.4 and 131.4 Å, respectively. The highest strength sample F has the shortest long-axis radius, whereas the weakest strength sample A has the longest long-axis radius. The size of the ellipsoidal scatterer is a little larger than Pauw's results (Pauw, Vigild, Mortensen, Andreasen & Klop, 2010), but is very close to Dobb's results (Dobb *et al.*, 1979). However, we have to mention that these values are affected by analyzing method and preparation process.

The radius of the spherical microvoids decreases as the strength increases (Fig. 5*d*). As mentioned above, samples A, B and C have obvious isotropic scattering and anisotropic scattering, while D, E and F have only evident anisotropic scattering. Therefore, spherical microvoids were taken into account only in samples A, B and C, and the radii of the spherical microvoids in these samples are 42.3, 38.5 and 36.7 Å, respectively. There are no obvious spherical microvoids in samples D, E and F, so the radii of the spherical microvoids in samples D, E and F is reported as zero in Table 3 and these samples are not included in Fig. 5(*d*).

Results reported elsewhere also show two kinds of scatterer, a smaller one and a larger one, or an isotropic one and an anisotropic one. Davies *et al.* (2008) found isotropic scattering in the core of an aramid (Kevlar29 from DuPont) and anisotropic scattering in the shell of the fiber. Aerts (1991) also found different kinds of scatterer in the core and shell of an aramid fiber. Results from Grubb *et al.* (1991) support the fact that the scatterer could be described by a bimodal distribution of sizes, but Grubb *et al.* thought that the entire scattering signal contribution came from the fibril rather than the microvoid and the fibril. It has been accepted that the fibril is parallel to the fiber axis, which means that the scattering signal will be perpendicular to the fiber axis and totally anisotropic. On account of the isotropic scattering in our results, there is much more reason to believe that spherical microvoids are present in the aramid fiber. Pauw, Vigild, Mortensen, Andreasen & Klop (2010) also support the notion of a bimodal distribution – where a larger ellipsoid represents the fibrillar structure while a smaller ellipsoid stands for the microvoid – but Pauw *et al.* did not found isotropic scattering in their aramid fiber.

The variance of the distribution and the instrument parameters all blur the scattering pattern. In the adapted model, we split these two kinds of effects by introducing instrument parameters into the two-dimensional SAXS model. The variance of the distribution becomes much smaller than that in Pauw's paper (of the order of thousands to tens of thousands of ångström; Pauw, Vigild, Mortensen, Andreasen & Klop, 2010) when we introduce instrument parameters, such as point spread function and beam profile, to the adapted model (less than 100 Å), which indicates that the adaptation is meaningful.

In general, as the strength increases, the ellipsoidal microvoid in the sample becomes smaller; the same is true of the spherical microvoid, whose radius varies from 42.3 to 38.5 to 36.7 Å, and finally disappears. The long axis of the ellipsoidal microvoid is almost parallel to the direction of the fiber axis, regardless of the performance of the aramid fiber.

The mechanical properties of the fiber were affected by the presence of microvoids, which coincide with the region of stress concentration. When tensile force was applied to the fiber, the aramid fiber fractured from the microvoid when the tensile force exceeded the threshold value of fracture force. This phenomenon is usual in various kinds of fiber, such as the fracture of the carbon fiber (Zhu *et al.*, 2012). Fig. 6 is a schematic diagram of an aramid fiber, where the aramid is composed of fibril and microvoid. The fibrils are represented by the yellow cylinders and the microvoids are represented by the white ellipsoids and spheres. When the microvoid becomes larger, the cross-sectional area becomes smaller, which results in the reduction of the tensile strength.

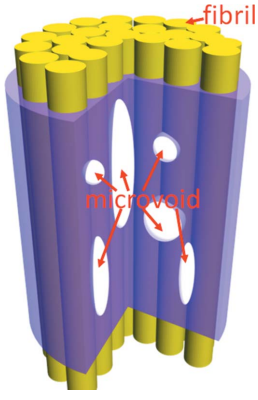

Figure 6
Schematic diagram of an aramid fiber.

5. Conclusions

In this paper, Pauw's scattering model has been adapted by introducing the orientation parameters of the zenith and azimuthal angle distributions and instrumental parameters such as point spread function and beam profile function to the model. SAXS data of aramid fibers with different mechanical properties were collected. The microvoid parameters of those samples were extracted from the scattering pattern by the adapted two-dimensional full pattern fitting method. The results show that the microvoids in the aramid fiber have a direct impact on its strength: the greater the number of spherical microvoids and the larger the ellipsoidal microvoids, the weaker the aramid fiber. Spherical microvoids have a more profound effect on the strength of an aramid fiber than ellipsoidal microvoids. The adapted two-dimensional full pattern fitting method is a valid tool to extract structural information from the oriented scattering pattern.

This work was supported by the 973 Program (grant No. 2011CB605604), the National Natural Science Foundation of China (grant Nos. 10979006, 10835008 and 11179027), the Innovation Project of the Chinese Academy of Sciences (KJCX2-YW-N39), the 863 Project (2009AA03Z513), the Opening Foundation of Shenzhen Key Laboratory of Functional Polymers (FP20120012), the Natural Science Foundation of Shenzhen University (grant No. 201204), the Shandong Taishan Talent Project and the Shenzhen Basic Research Project (JCYJ20120614085820810). The authors also thank Dr B. R. Pauw for valuable discussions on the two-dimensional SAXS model, and Dr Xiuhong Li, Dr Fenggang Bian, Dr Yuzhu Wang, Dr Feng Tian, Dr Zhou and Dr Ping at SSRF for assistance in SAXS testing.

References

Aerts, J. (1991). *J. Appl. Cryst.* **24**, 709–711.
Davies, R. J., Koenig, C., Burghammer, M. & Riekel, C. (2008). *Appl. Phys. Lett.* **92**, 101903.
Dobb, M., Johnson, D., Majeed, A. & Saville, B. (1979). *Polymer*, **20**, 1284–1288.
Du, H. & Voss, K. J. (2004). *Appl. Opt.* **43**, 665–670.
Engel, M., Stühn, B., Schneider, J. J., Cornelius, T. & Naumann, M. (2009). *Appl. Phys. A Mater.* **97**, 99–108.
Fischer, S., Diesner, T., Rieger, B. & Marti, O. (2010). *J. Appl. Cryst.* **43**, 603–610.
Gardner, K. H., English, A. D. & Forsyth, V. T. (2004). *Macromolecules*, **37**, 9654–9656.
Glatter, O. & Kratky, O. (1982). *Small Angle X-ray Scattering.* London: Academic Press.
Grubb, D. T., Prasad, K. & Adams, W. (1991). *Polymer*, **32**, 1167–1172.
Hermans, P. H., Heikens, D. & Weidinger, A. (1959). *J. Polym. Sci.* **35**, 145–165.
Hindeleh, A. & Abdo, S. (1989). *Polymer*, **30**, 218–224.
Hindeleh, A. M., Halim, N. A. & Ziq, K. A. (1984). *J. Macromol. Sci. Phys.* **23**, 289–309.
Humbert, S., Lame, O., Chenal, J. M., Rochas, C. & Vigier, G. (2010). *Macromolecules*, **43**, 7212–7221.
Kortleve, G. & Vonk, C. G. (1968). *Kolloid Z. Z. Polym.* **225**, 124–131.
Kotera, M., Nakai, A., Saito, M., Izu, T. & Nishino, T. (2007). *Polym. J.* **39**, 1295–1299.
Liu, J., Cheng, S. & Geil, P. (1996). *Polymer*, **37**, 1413–1430.
Mark, H. F. (2004). *Encyclopedia of Polymer Science and Engineering*, 3rd ed. New York: Wiley-Interscience.
Mooney, D. A. & MacElroy, J. (2004). *Chem. Eng. Sci.* **59**, 2159–2170.
Northolt, M. G. (1981). *Br. Polym. J.* **13**, 64–65.
Northolt, M. G. & van Aartsen, J. J. (1977). *J. Polym. Sci. Part C Polym. Symp.* **58**, 283–296.
Northolt, M. & Hout, R. (1985). *Polymer*, **26**, 310–316.
Pauw, B. R., Vigild, M. E., Mortensen, K., Andreasen, J. W. & Klop, E. A. (2010). *J. Appl. Cryst.* **43**, 837–849.
Pauw, B. R., Vigild, M. E., Mortensen, K., Andreasen, J. W., Klop, E. A., Breiby, D. W. & Bunk, O. (2010). *Polymer*, **51**, 4589–4598.
Perret, R. & Ruland, W. (1970). *J. Appl. Cryst.* **3**, 525–532.
Plazanet, M., Fontaine-Vive, F., Gardner, K. H., Forsyth, V. T., Ivanov, A., Ramirez-Cuesta, A. J. & Johnson, M. R. (2005). *J. Am. Chem. Soc.* **127**, 6672–6678.
Pontoni, D., Narayanan, T. & Rennie, A. R. (2002). *J. Appl. Cryst.* **35**, 207–211.
Ran, S., Fang, D., Zong, X., Hsiao, B., Chu, B. & Cunniff, P. (2001). *Polymer*, **42**, 1601–1612.
Rao, Y. (2001). *Polymer*, **42**, 5937–5946.
Ruland, W. (1977). *Colloid Polym. Sci.* **255**, 417–427.
Ruland, W. (1978). *Colloid Polym. Sci.* **256**, 932–936.
Stribeck, N. (2004). *Macromol. Chem. Phys.* **205**, 1455–1462.
Stribeck, N. (2007). *X-ray Scattering of Soft Matter.* Berlin, Heidelberg: Springer-Verlag.
Stribeck, N., Nöchel, U., Fakirov, S., Feldkamp, J., Schroer, C., Timmann, A. & Kuhlmann, M. (2008). *Macromolecules*, **41**, 7637–7647.
Stribeck, N. & Ruland, W. (1978). *J. Appl. Cryst.* **11**, 535–539.
Suhonen, H., Fernández, M., Serimaa, R. & Suortti, P. (2005). *Phys. Med. Biol.* **50**, 5401–5416.
Thünemann, A. F. & Ruland, W. (2000). *Macromolecules*, **33**, 1848–1852.
Uesugi, K., Hoshino, M. & Yagi, N. (2011). *J. Synchrotron Rad.* **18**, 217–223.
Vonk, C. G. (1979). *Colloid Polym. Sci.* **257**, 1021–1032.
Young, R. J., Lu, D., Day, R. J., Knoff, W. F. & Davis, H. A. (1992). *J. Mater. Sci.* **27**, 5431–5440.
Zhu, C., Liu, X., Yu, X., Zhao, N., Liu, J. & Xu, J. (2012). *Carbon*, **50**, 235–243.